Hi-Fi fMRI: High-resolution, fast-sampled and sub-second whole-brain functional MRI at 3T in humans

Benedetta Franceschiello[1,2,3,4,*], Simone Rumac[2], Tom Hilbert[2,5,6], Matthias Nau[7], Martyna Dziadosz[1,2,3], Giulio Degano[9], Christopher W. Roy[2], Anna Gaglianese[2,3], Giovanni Petri[8], Jérôme Yerly[2,4], Matthias Stuber[2,4], Tobias Kober[2,5,6], Ruud B. van Heeswijk[2], Micah M. Murray[2,3,4,+], and Eleonora Fornari[2,4,+]

[1]Institute of Systems Engineering, School of Engineering, HES-SO Valais-Wallis, Sion, Switzerland
[2]Department of Radiology, Lausanne University Hospital and University of Lausanne, Lausanne, Switzerland
[3]The Sense Innovation and Research Center, Lausanne and Sion, Switzerland
[4]CIBM Center for Biomedical Imaging, Lausanne, Switzerland
[5]Advanced Clinical Imaging Technology, Siemens Healthineers International AG, Lausanne, Switzerland
[6]LTS5, École Polytechnique Fédérale de Lausanne (EPFL), Lausanne, Switzerland
[7]Laboratory of Brain and Cognition, National Institute of Mental Health, National Institutes of Health, Bethesda MD, USA
[8]CENTAI, Corso Inghilterra 3, Turin, Italy
[9]Department of Psychology, Faculty of Psychology and Educational Sciences, University of Geneva, Geneva, Switzerland
[*]Corresponding author: benedetta.franceschiello@hevs.ch
[+]Shared senior authorship

ABSTRACT

Functional magnetic resonance imaging (fMRI) is a methodological cornerstone of neuroscience. Most studies measure blood-oxygen-level-dependent (BOLD) signal using echo-planar imaging (EPI), Cartesian sampling, and image reconstruction with a one-to-one correspondence between the number of acquired volumes and reconstructed images. However, EPI schemes are subject to trade-offs between spatial and temporal resolutions. We overcome these limitations by measuring BOLD with a gradient recalled echo (GRE) with 3D radial-spiral phyllotaxis trajectory at a high sampling rate (28.24ms) on standard 3T field-strength. The framework enables the reconstruction of 3D signal time courses with whole-brain coverage at simultaneously higher spatial (1mm^3) and temporal (up to 250ms) resolutions, as compared to optimized EPI schemes. Additionally, artifacts are corrected before image reconstruction; the desired temporal resolution is chosen after scanning and without assumptions on the shape of the hemodynamic response. By showing activation in the calcarine sulcus of 20 participants performing an ON-OFF visual paradigm, we demonstrate the reliability of our method for cognitive neuroscience research.

1 Introduction

The discovery of the blood-oxygen-level-dependent (BOLD) signal in the 1990s (1; 2; 3; 4) made it possible to non-invasively measure brain activity with MRI, which has been a major driver of human cognitive neuroscience since then. The introduction of BOLD imaging has removed the need for contrast agents or radiolabeled isotopes, and the subsequent introduction of echo-planar imaging (EPI) (5; 6) made it possible to image the entire brain with reasonable compromises in terms of speed, spatial resolution, and sensitivity to artifacts (4; 7). However, like any other technique, BOLD functional imaging has its limitations, and users often need to compromise between temporal versus spatial resolutions alongside the extent of brain coverage (i.e., field of view; FoV) (8). Without acceleration techniques, baseline EPI schemes take 2–3s to obtain 3mm isotropic images of the whole brain at 3T magnetic field strength (9). Consequently, EPI schemes are generally optimized with acceleration techniques. For instance, simultaneous multi-slice (SMS) acquisitions (10) such as multiband techniques (11; 12) reach whole-brain coverage in 0.5-1s and with around 2mm isotropic spatial resolution (9). Often, acceleration techniques decrease the signal-to-noise ratio and increase the likelihood of degrading artifacts (13; 14), thereby limiting data quality in research and clinical applications. For example, a recently proposed acquisition approach based on a 3D radial sampling trajectory (15) improved BOLD sensitivity but still required compromises between temporal and spatial resolution. For instance,

approaches that allow imaging hemodynamic responses at high temporal resolution require lower spatial resolution or smaller coverage (14; 16; 17; 18). Likewise, it is possible to use radial-Cartesian (stack of radials) sampling patterns to acquire a single slice at ultra-high spatial resolution, although it requires a long acquisition time (2.4s) (19). Moreover, recent technical advances have been shown to measure more fine-grained brain dynamics based on the local influence of electric activity on the magnetic field (20; 21), which however rely on ultra-high field strength (9.4T), are prone to motion artifacts, and were tested only in anesthetized animals on well-studied neurobiological systems (i.e., visual sensory cortices or whisker fields in rodents)(20; 22). Such approaches have been referred to as ultra-fast fMRI and can be powerfully combined with modeling or optogenetic techniques (23; 24). Nevertheless, up-scaling such techniques to the human brain to measure BOLD activity remains extremely challenging.

Here, we introduce a new and broadly applicable framework that achieves a k-space acquisition sampling rate of 28.24ms, greatly exceeding traditional approaches on standard clinical MRI systems. The acquired images cover the entire brain at a high spatial resolution (1mm isotropic) with limited spatial distortions. Moreover, the percent signal change curve can be studied at different temporal resolutions (up to 250ms). Temporal resolution is set at reconstruction (that is, after scanning), hence avoiding assumptions about the shape of the hemodynamic response. Our novel fMRI framework therefore overcomes multiple critical limitations of the quasi-standard and widely used EPI-based BOLD imaging technique, and promises studies of human brain dynamics at a new level of detail.

2 Results

2.1 Higher spatial and temporal resolutions in BOLD contrast maps with increased statistical power

Twenty healthy volunteers in a 3T clinical scanner (MAGNETOM Prisma^{fit}, Siemens Healthcare, Erlangen, Germany) underwent an established blocked-design flickering checkerboard visual stimulation experiment (25), fig. 1, top row left. Data were acquired using an uninterrupted gradient recalled echo (GRE) sequence with a 3D radial-spiral phyllotaxis sampling trajectory (26) (fig. 1, top row center), with a temporal sampling rate of 28.24ms and 1mm^3 spatial resolution. The versatility of the framework lies in the fact that single readouts acquired in the image sampling space (k-space) can be grouped ("binned") flexibly together, as well as retrospectively discarded if necessary. The rationale behind this binning strategy can be understood as follows: single readouts contribute to the image-reconstruction and signal analyses with a precision of 28.24ms. Noisy readouts are excluded, hence correcting for the head's rigid-body motion in frequency domain and preempting their degrading contribution to the reconstruction. This allows researchers to control for motion artifacts and other experimental outliers before reconstruction, rather than retrospectively correcting for them in preprocessing or accounting for them in analysis.

An additional, critical advantage over traditional methods is that the framework allows computing the percent signal change associated with an experimental manipulation at a finer temporal scale. Furthermore, T_2^* BOLD contrast maps are computed at the single-participant level as the mathematical difference $\|ON - OFF\|$. Here, ON refers to the volume obtained through reconstruction of all readouts acquired during the stimulus-evoked hemodynamic response function peak (assumed to reach plateau after 5 seconds after stimulus onset and lasting for 10 s in correspondence with our stimulation), while OFF refers to the volume obtained unifying all readouts acquired during the resting phase of the response (assumed to be 25-35 s post-stimulus) (27).

The obtained contrast maps replicate their classical counterpart such as those estimated via a canonical General Linear Model (GLM) analysis and EPI (28; 29). Conversely, the framework does not rely on the GLM's assumptions (such as experimental design constraints, normal distribution of variance, linearity, hemodynamic response function), and importantly, performing at a finer temporal scale. We generated activation contrast maps with a whole-brain coverage for each participant individually, consistently showing a highly localized activation at the calcarine sulcus along the occipital lobe, as it would be expected with the task (see fig. 1, bottom row, center for a single participant). Moreover, these contrast maps were generated at 1 mm^3 spatial resolution, and ms sampling rate, substantially better than traditional approaches. We performed voxel-wise group-level analysis (fig. 1, bottom row right), confirming the single-participant results. Moreover, the use of a radial k-space acquisition pattern mitigates the well-characterized distortions of areas in the medial temporal lobe and orbitofrontal cortex. These distortions are typically showcased by EPI images due to the prolonged echo readout trains (see an exemplary subject in fig. 5). We then used the same data to reconstruct volumes at different temporal resolutions, (fig. 1, top row right - temporal Signal to Noise Ratio -tSNR), grouping the signal across all trials at 250ms, 500ms (bottom row left, fig. 1), 1s and 2.5s temporal resolutions, respectively. As expected, the tSNR decreased for higher temporal resolutions, but it remained around 150 even with a temporal resolution of around 250ms(30). This suggests that our framework could in principle be successfully applied at even higher temporal resolutions than 250ms. Our framework permits to treat fMRI acquisition, up to now acquired and processed at 2-3Hz, as a fast-sampled signal where signal processing techniques in the frequency domain can be now applied. Such strategies, allow for better control over which raw data enter the analysis pipeline with millisecond precision, allowing for improved performance of artifact/noise corrections and the derivation of activations more generally. This was not possible using previously existing methods.

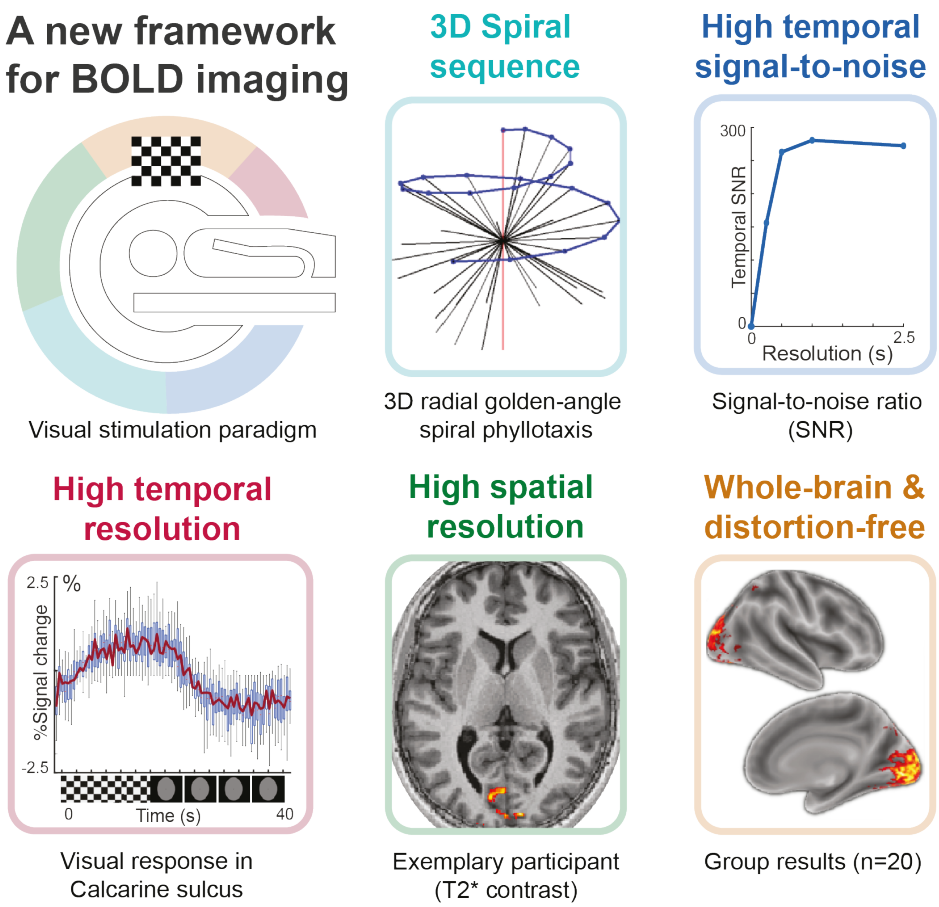

Figure 1. Graphical summary. Data were acquired using an uninterrupted gradient recalled echo (GRE) sequence with a 3D radial spiral phyllotaxis sampling trajectory (top center) and a sampling rate of 28.24ms (time needed to acquire a single spiral, i.e., interleaved) during a block design visual stimulation (ON vs. OFF flickering checkerboard). The same acquisition is then used to reconstruct the volume at different temporal resolutions, grouping the signal across all trials at temporal resolutions of 250ms, 500ms (bottom-left), 1s and 2.5s, respectively. The tSNR (temporal Signal to Noise Ratio) decreased for increasing temporal resolution (250ms), but remained high at around 150ms. This suggests that this framework could be successfully applied to even shorter temporal resolutions (top right). The bottom-central figure demonstrates the highly localized activation we obtain at the single-participant level (calcarine, occipital cortex, at $1mm^3$ spatial resolution). Finally, we show the result at the group-level (bottom-right), obtained via a paired t-test ($p < 0.001$, extent threshold of 100 contiguous voxels).

2.2 Percentage BOLD-signal change in the visual cortex with a temporal resolution up to 250ms

First, the ON vs. OFF statistical contrasts demonstrate the regional specificity of the activations we obtain with our framework (fig. 1). Percent signal change was reliably extracted at different temporal resolutions within the calcarine sulcus, which includes primary and secondary visual areas (average across 33 trials at temporal resolutions of 250ms, 500ms, 1s and 2.5s in a corresponding number of bins of 160, 80, 40, and 16). As expected, we were able to retrieve a percent signal change (1%, fig. 2 (a), left) indicating a consistent hemodynamic response in the calcarine sulcus (standard deviation of the signal 0.43%) across different temporal resolutions. By contrast, no reliable activation was observed in any of the other control ROIs, including the superior temporal lobe and precuneus (<0.05%, fig. 2, b). These results replicate the well-known response to visual stimulation in the calcarine sulcus (28; 29; 31; 32). Despite the increased number of bins (and conversely the decreased number of readouts per bin), the recorded percent signal change remained stable, while the temporal signal-to-noise ratio (tSNR) remained above 150(30) even for higher temporal resolutions (250ms), see (fig. 1, tSNR). Importantly, these results establish an experimental basis for investigating the trade-off between high temporal resolution BOLD fMRI reconstructions and the sparsity of bins.

2.3 Contributions of compressed-sensing and sparsity in T_2^*-weighted BOLD contrast in the visual cortex

Inference at the group level was computed via a paired-t-test ($p < 0.001$, extended threshold of 100 contiguous voxels) and show canonical activation in the calcarine sulcus as well as the lateral geniculate nuclei (33; 34). This is displayed in fig. 3, first row ($\sim$23k (a.u) in voxel intensity of BOLD map threshold-free cluster enhancement (TFCE)-corrected (35)) which is based on the 33x2 reconstruction, i.e. 5D reconstruction performed by using the whole acquisition of all 33 trials (hereafter referred to as "5D-all"), see also fig. 5 for exemplar single-participant data from the lateral geniculate nuclei (supplementary material, fig. 5) The first three dimensions of the 5D-all reconstruction reflect space (voxels), the fourth dimension reflects the number of trials, and the fifth reflects the estimated hemodynamic response (ON and OFF).

To explore the role of sparsity (i.e. the number of lines used for reconstructing) and compressed-sensing (CS) (36), we report the group-level statistical inference also for the 17x2 reconstruction, i.e., a 5D reconstruction performed by using half of the acquired trials (i.e., half of the readouts, fig. 3, second row; hereafter referred to as "5D-half"), as well as the group-level statistical inference for the $T_2{}^*$-weighted BOLD contrast derived from the 4D real time (RT) reconstruction (16 temporal bins, fig. 3, third row; hereafter referred to as "4D-all", where the fourth dimension is the length of one trial chunked at different temporal resolutions), and finally from the reconstruction performed without the application of the CS algorithm ($\sim$10k (a.u) in voxel intensity of BOLD map TFCE-corrected). In this case, the readouts are placed in a Cartesian grid, but no regularization is applied to explore shared information across nearby bins (fig. 3, fourth row; hereafter referred to as "No-CS"). Table 1 reports the achieved reconstruction times, with up to 1h30 for the 4D-all.

The same significance in terms of activation (paired-t-test, $p < 0.001$, extended threshold of 100 contiguous voxels) is reached in the 5D-all, 5D-half, and 4D-all cases, although the activation maps show decreases in signal intensity. A very low and noisy signal is obtained when the compressed-sensing reconstruction is not performed (i.e., the No-CS reconstruction approach). These results provide a preliminary indication of the role of CS reconstruction in reducing the amount of data that need to be used during reconstruction to retrieve % signal change within the volumes.

We quantitatively compared, on a voxel-by-voxel basis, the spatial superposition and intensities of activations across reconstruction approaches with respect to the 5D-all method (see fig. 3, fifth row). Blue-toned voxels indicate where there was either an activation observed in the 5D-all reconstruction, which was not observed in the comparison reconstruction approach, or where activations were observed in both reconstructions, but with greater intensity in the 5D-all reconstruction. Blue voxels thus indicate where the 5D-all reconstruction outperformed the comparison reconstruction in extent and/or intensity. Red voxels, by contrast indicate the opposite; i.e., where the comparison reconstruction outperformed the 5D-all approach. The histograms show these differences throughout the brain volume. The x-axis shows the difference in signal intensity, whereas the y-axis shows the number of voxels that attain such a difference.

Compared with the 5D-all reconstruction, the 5D-half approach displays activation patterns in the visual cortex, although with generally lower intensity (difference in voxel intensity between 0 and 10'000 (a.u) of BOLD map TFCE-corrected). Compared with the 5D-all reconstruction, the 4D-all approach also resulted in activation at generally the same loci, but with far lower intensity (fig. 3, center). Finally, comparing the 5D-all and No-CS approaches revealed that if CS is not applied, spurious patterns (red) appear throughout the volume, and the difference in the signal increases (25'000 (a.u) of BOLD map TFCE-corrected), see fig. 3, right.

3 Discussion

We introduced a new framework that comprehensively overcomes the current limitations of fMRI research. We successfully acquired whole-brain signals on a standard 3T clinical scanner while preserving a $1mm^3$ resolution in space, and a high, sub-second temporal resolution. Our approach allows organizing single k-space readouts in a flexible manner to either retrieve specified signals at different temporal scales or alternatively be discarded to remove those affected by artifacts, including but

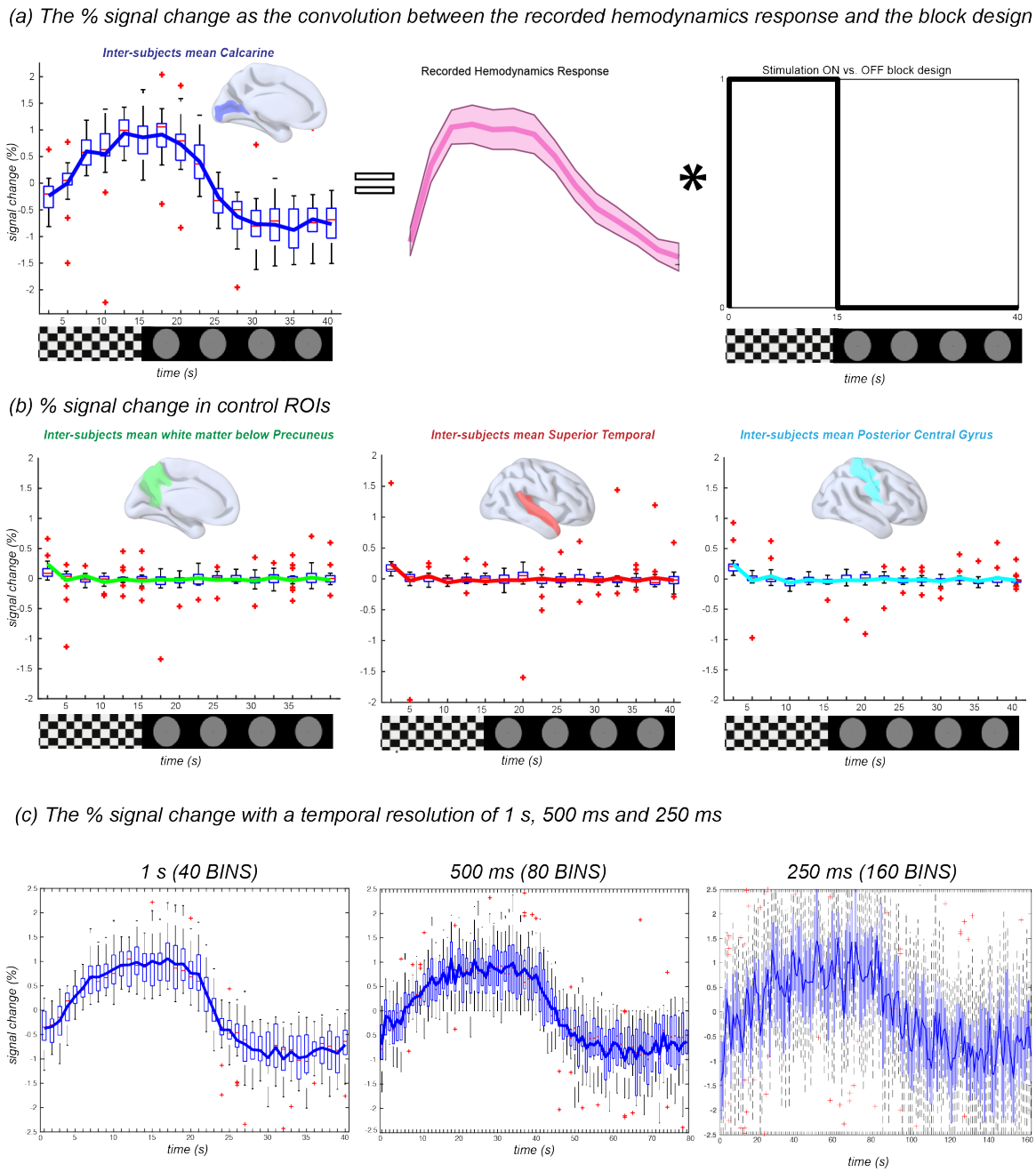

Figure 2. Percentage BOLD-signal change in the visual cortex with a temporal resolution up to 250ms. In the top line, we show the percent signal changes in the calcarine sulcus, estimated from 4D reconstruction at a temporal resolution of 2.5s (16 bins). We retrieve the canonical hemodynamic response (center) as extracted by deconvolving the block design (right). The middle row reports the extraction of the percent signal change in different ROIs (Precuneus - green, Temporal Lobe - red, Posterior Central Gyrus - cyan). As expected, activity within these ROIs remains below significance threshold (<0.05%) as these regions are not a priori expected to respond to visual stimuli. The bottom row contains the extracted percent signal change at different temporal resolutions (averaged across trials at a temporal resolution of 1s, 500ms, or 250ms in a corresponding number of 40, 80, or 160 bins). Despite the increased number of bins, the recorded percent signal change remains stable, while the temporal signal to noise ratio remains above 150, even in the higher temporal resolution reconstruction (250ms) - see fig. 1.

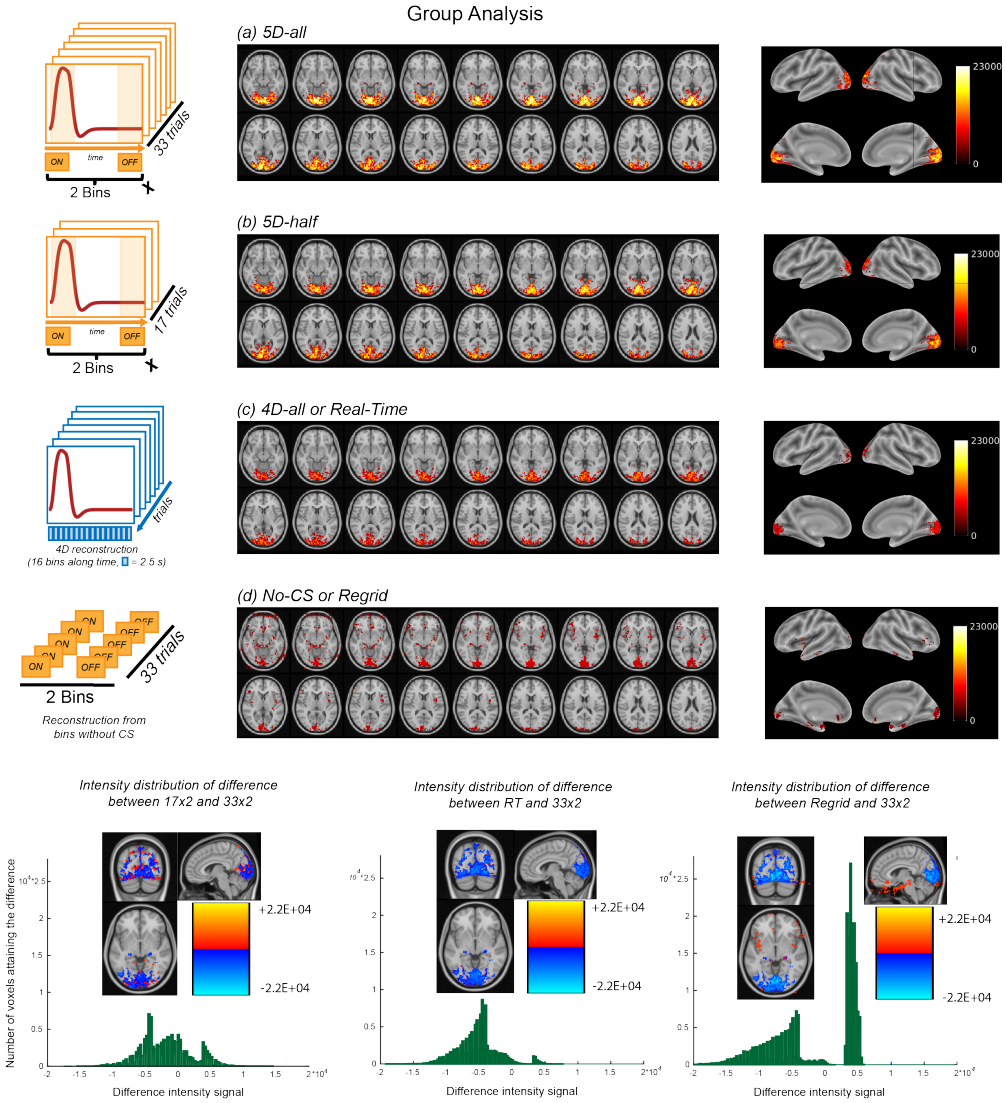

Figure 3. T_2*-weighted BOLD contrast and quantitative comparison of reconstruction approaches Here, we present the inference at the group level computed as a paired-t-test ($p < 0.001$, extended threshold of 100 contiguous voxels) with different numbers of readouts used for reconstruction. The first row presents results obtained by using all readouts (all 33 trials, 5D-all), where we can observe activation in the calcarine sulcus (∼23k (a.u) in voxel intensity of BOLD map TFCE-corrected, see colorbar). The second row contains the results for the 5D-half reconstruction (i.e., using half of the readouts), and the third row the 4D Real-time (4D-all) reconstruction (with all readouts). The maps show that we reach the same significance in the 5D-half case, as well as in the 4D-all, although with an observed decrease in the signal intensity. The fourth row presents the inference at the group level without the application of the compressed-sensing algorithm (No-CS), where no regularization is applied. In this case, we observe highly non-uniform patterns (∼10k (a.u) in voxel intensity of BOLD map TFCE-corrected). The fifth row presents an histogram comparison where we plot in green the intensity of the difference between each performed reconstructions (5D-half, 4D-all, No-CS) relative to the referenced reconstruction (5D-all). Blue-intensity voxels in the anatomical insets indicate either an activation present in the 5D-all reconstruction, but not visible in the other reconstructions, or voxels which activate in both reconstructions but at different intensities. Red voxels in the anatomical insets refer to activation present in the comparison reconstruction, but not in the 5D-all.

not limited to head motion. While a single readout is insufficient to reconstruct a full volume at present, we have demonstrated that our acquisition and reconstruction strategies exceed the spatial resolution and activation precision of traditional EPI-based approaches (9) (see fig. 3), while limiting traditional EPI distortion (see fig. 5, supplementary material). Importantly, our approach has the potential to account for physiological artifacts, such as respiration and heartbeat, at the image reconstruction stage, allowing to reconstruct functional volumes and hemodynamic time courses independent of such sources of noise. This opens up –for the first time in humans– the possibility of disentangling components(37) participating to the observed percent signal change at a high temporal scale (sampling rate of 28.24ms).

To the best of our knowledge, this is the first time an fMRI protocol allows to reach a recorded (averaged) temporal resolution of 250ms while still retaining both whole-brain coverage and small voxel size (1 mm^3) in humans. Up to now, measuring brain dynamics at a high temporal resolution with MRI (20; 38) was achieved only by compromising other factors (e.g., brain coverage, laminar fMRI). For comparison, at a field strength of 3T as used in the present work, current multi-slice EPI approaches reach 0.5-1s with whole-brain coverage with $3mm^3$ spatial resolution (9), unless further accelerated using methods that increase the risk and severity of artifacts. Our framework avoids compromising between high temporal resolution, spatial resolution, and coverage. Further developments in the reconstruction algorithm together with the use of CS in reconstructing the signal would be necessary to further improve the temporal resolution below 250ms (at present, this corresponds to the maximum computational cost that can be handled by typical high performance computing systems) and at a single-trial level.

From an analysis standpoint, our framework avoids assumptions (e.g., HRF shape) inherent to the most wide-spread analyses of fMRI data (e.g., the GLM) at the single-participant level. Instead, the $T_2{}^*$ weighted activation maps from each participant in response to the visual stimulus are computed as the signal contrast that arises after stimulus onset across trials. $T_2{}^*$-weighted maps are computed as a difference between the volume reconstructed by combining all readouts acquired during the activation state of the brain minus the volume reconstructed by combining all readouts acquired during the resting state of the brain. This does not undermine the utility of the GLM, which will be integrated in our approach to perform more complex cognitive paradigm designs and to further improve sensitivity of our method.

From the acquisition standpoint, it has been known that spiral sampling patterns are less sensitive to motion and geometric distortions compared to Cartesian trajectories (EPI imaging), and have improved signal recovery, especially in frontal and parietal regions (39; 40). Here, we used a 3D radial - spiral phyllotaxis trajectory (26) for BOLD fMRI, and tested it as a component of our framework: we retrieve the desired activation pattern, validating our sequence's use in BOLD functional imaging. Notably, our 5D-all reconstruction approach was able to successfully detect significant activations at the group-level within thalamic structures (i.e. the lateral geniculate nuclei, see 5, in addition to prominent clusters in the occipital lobe. While further refinements are feasible and likely required, the present framework already functionally assessed small thalamic nuclei (33; 34; 41; 42), while nonetheless retaining whole-brain coverage and high spatio-temporal resolution. From the reconstruction standpoint, we validated the use of CS in retrieving the expected activation even when shortening the reconstruction (5D-half), reducing the acquisition time to 11 minutes, or when performing a quicker reconstruction (1h30m) to analyze the hemodynamic response function of the % signal change (via the 4D-all reconstruction). Our results and those of other similar approaches in the field of CS applied to MRI (43; 44) suggest that the required number of trials (and therefore the computational time) could be further reduced in the future.

The combination of all these advancements has the potential to innovate the current state of the art of human fMRI: examining human brain activity at high spatial and high temporal resolution in a motion-robust manner, with whole-brain coverage and without distortions, can fundamentally change the breadth of studies that can be conducted. For example, it may allow studies of new populations of participants, who tend to move during scanning (e.g., patients, neonates, children, and elderly). The framework's robustness against motion and other common sources for artifacts reduces, or may even eliminate, the need for sedatives and similar products, while still obtaining high-quality structural and functional data. The flexible grouping and analysis of temporal bins furthermore allows researchers to more readily disentangle activation linked to specific stages of cognitive processing, for example between pre-stimulus preparation, stimulus perception, behavioral response etc, for example by the influence of these trial stages on the shape of the hemodynamic signals. Given a sufficient number of trials, one can even generate specific activation maps aligned to stimulus onset in a manner akin to practices in time-resolved techniques such as M/EEG (45; 46). Moreover, the combination of high spatial resolution and whole-brain coverage may allow new analyses of layer-specific BOLD responses, for example to estimate the whole-brain connectivity fingerprint of individual layers (e.g., (47). In this regard, our framework likewise may facilitate resolution of longstanding open questions with regard to neuro-vascular coupling (48; 49; 50; 51), moving towards a more quantitative analysis of the BOLD signal components: by acquiring readouts at a high-sampling rate, one can perform separate frequency analyses and extract physiological information, reorganizing the readouts according to different heartbeat states, respiratory states and so on. In this way, BOLD activation will not only be coupled with physiology, but reconstructed *according to* physiological states, allowing to intrinsically investigate the real contributors to hemodynamic activity. Another major advantage of our framework compared to the current state-of-the-art is that one may use the same data for functional- and structural analyses (including cortical parcellations and surface inflation) by

acquiring and (consequently binning data) according to different echos. By alleviating the need to acquire separate structural and functional scans, our approach avoids issues inherent to the co-registration of these different data types, which constitutes a high-risk source for error. This could be especially important for paradigms that require a large number of participants, and therefore a high number of individual data-quality checks (e.g., brain-wide association studies,(52)). It may further allow creating regions-of-interest masks based on anatomical landmarks using the same data that is used for functional analyses, notably using independent criteria. Finally, our approach could also be extended to organs other than the brain for which MRI imaging remains challenging due to bulk motion, breathing, or heart-beat (e.g., the spinal cord) (53; 54; 55), and those where motion encompasses key behavioral information, as in the eye (56). The latter could be especially interesting when combined with a set of techniques that resolve for motion in those organs (57; 58; 59). While the research opportunities created by our framework far exceed the few examples mentioned here, they illustrate that our approach constitutes a major advance in functional BOLD imaging, and that it has the potential to fundamentally re-define which research questions are addressable with fMRI for cognitive neuroscience and clinical research (52).

4 Online Methods

4.1 Participants and visual stimulation

Twenty healthy volunteers (sex: 11 females, 9 males) were scanned in a 3T clinical scanner (MAGNETOM Prisma^{Fit}, Siemens Healthcare, Erlangen, Germany) with a 64-channel head coil. Visual stimuli were back-projected onto a mirror attached to the head coil, with a total distance between the participants' eyes and the screen of 102 cm. The study protocol received approval by the cantonal ethics committee (protocol number $2018-00240$). The visual field on the mirror spanned 18°. The stimulation protocol followed a block design of 33 trials of 40 s. This many trials repetitions were due to the fact that the technique is still at a prototype level. One trial entailed a 15s ON phase (8Hz flickering checkerboard) followed by a 25s OFF phase (full-field and uniform grey image), see fig. 4, second row. This sequence allows BOLD signal to reach its peak (after $\sim$5s) and to return to baseline (after $\sim$30s). A small centered attentional cue, changing color across time was placed at the center of the screen to help participants maintaining fixation. Participants were asked to maintain the eyes relaxed and to minimize blinking and movements. Eye movements were tracked using an eye-tracking system (EyeLink 1000Plus, SR Research) synchronized with the MRI scanner via Syncbox (NordicNeuroLab). An Experiment builder (EyeLink) program was developed and used to control the calibration of the Eye-Tracker from outside the scanner room and to correctly synchronize the different hardware components of the experiment. Eye movement trajectories (of the right eye) were recorded using infrared light, with a sampling rate of 1000 Hz, through a mirror positioned inside the scanner bore, replacing the standard head-coil mirror usually available, which is not infrared compatible.

4.2 Acquisition

Data were acquired using a prototype uninterrupted gradient recalled echo (GRE) sequence with a 3D radial - spiral phyllotaxis sampling trajectory (26; 60) that enables uniform k-space coverage in all bins, see fig. 4, first row. The acquisition and the visual stimulation were synchronized via a Syncbox (NordicNeuroLab). A total of 46,772 readouts (segments=22, shots=2100) were acquired with a temporal resolution of 28.24ms (TR needed for a single readout in the uninterrupted sequence), TE=25ms, FoV=192mm^3 with 1mm^3 isotropic resolution, FA=12°, and TA=22min. A high resolution anatomical T1 weighted volume (MPRAGE, TE= 2.43ms, TR=1890ms, TI=955ms, FA=9°, FOV=256x256, 192 slices, voxel=1 mm^3 isotropic) was acquired as basis for ROIs segmentation.

4.3 $T_2{}^*$-weighted BOLD contrast image Reconstruction and signal extraction, 5D-all and 5D-half and No-CS

To obtain the BOLD signal maps with different amounts of acquired data, all datasets were reconstructed three times. We performed 5D (x-y-z-rep-act dimensions, where rep refers to the 33 trials, i.e., the number of times the task was repeated and act refers to the ON or OFF phase of the estimated hemodynamics response) image reconstruction (61). The 5D reconstructions have been performed three times, each with different amount of k-space readouts: first with the total numbers of acquired readouts (5D-all), then with half of those (5D-half) and finally with all readouts but without applying any regularisation (No-CS). In the 5D reconstruction, the ON-phase was reconstructed by retaining readouts acquired over the 5-15s trial time interval (hemodynamic response reaches its plateau after 5s stimulus onset), and for the OFF-phase readouts acquired over the 30-40s trial time interval were retained, see fig. 4, block b (second row), orange boxes over the hemodynamic response curve (such ON vs. OFF volumes are reconstructed along the *act* dimension). All other readouts were discarded. The first two reconstructions were performed with a k-t-sparse SENSE algorithm(36) (image undersampling 20%), resulting in 66 3D volumes, see fig. 4, block c2, bottom right, orange reconstruction, first with the total number of lines acquired and then with half of it. In such cases, total variation regularization (see table 1 for parameters and reconstruction time) was applied along the rep dimension (number of trials), as readouts acquired during the same hemodynamic phase but across different trials share information, while

the different trials (N=33) were then combined via sum of squares. Motion correction translation and rotational coefficients were estimated using SPM12 (62) and used to correct the original k-space in all three reconstructions. $T_2{}^*$-weighted volume at the single participant level is computed as a pure mathematical difference between the sum of squared ON and OFF, i.e., $||ON - OFF||$. The inference at a group level was computed as a paired-t-test (p<0.001, extended threshold of 100 contiguous voxels) between volumes corresponding to the ON phase of the participants and those corresponding to the OFF one. Such analyses have been performed in all the three reconstructions mentioned above, as well as in the 4D-all described below, to explore the role of CS. We also computed histograms showing the distribution of intensity values of the differences between reconstructions. All reconstructions and analyses were performed in MATLAB (The MathWorks, Inc., Natick, MA, USA) on a workstation equipped with two Intel Xeon CPUs, 512GB of RAM, and an NVIDIA Tesla GPU. Time and parameters for the different reconstructions are presented in table 1.

4.4 Real-Time hemodynamic response image reconstruction, 4D-all

Temporal reconstructions were computed to track the hemodynamic signal evolution across time. Reconstructions were obtained by subdividing every trial into temporal bins of different temporal sizes: 2.5s, 1s, 500ms, 250ms, thus producing a four-dimensional reconstruction (x, y, z, t) comprised of respectively 16, 40, 80, 160 time frames (bins) along the signal evolution curve. After binning the data, the 3D volumes were reconstructed using a compressed-sensing-based algorithm (k-t sparse SENSE) where a Fourier Transform operator was employed to exploit the shared information between different time frames (along the temporal dimension, see table 1 for parameters). The reconstructed images were used to extract the evolution of the hemodynamic response in regions of interest (ROIs) averaged across all trials, see fig. 4, block c1, bottom right, blue reconstruction. Fourier transform regularisation was applied along the temporal dimension of the 4D-all reconstruction see fig. 4, block c1, bottom right, blue reconstruction. The hemodynamic response function has been therefore retrieved at different temporal resolutions.

4.5 Hemodynamic response extraction and group-level analysis

Bilateral Regions of interest (ROIs) were extracted using FreeSurfer (63) at the individual participant level and included the calcarine cortex (primary visual cortices), superior temporal sulci (primary auditory cortices), the postcentral gyrus (somatosensory cortices) and thalamic nuclei (lateral geniculate nuclei) of three exemplar participants (best percent signal change for these participants, see 5). The mean average signal across different trials in the ROIs was computed for each of the temporal bins (16, 40, 80, 160 bins), after registering the T1 map from which the ROIs were derived onto our 4D-all reconstruction via SPM12 (62). For displaying the recorded hemodynamic response, see light purple curve of fig. 2, center, outliers have been removed via Matlab outliers removal function, resulting in 2 excluded participants. Including outliers modifies the y-axis scale to $[-4, 4]$.

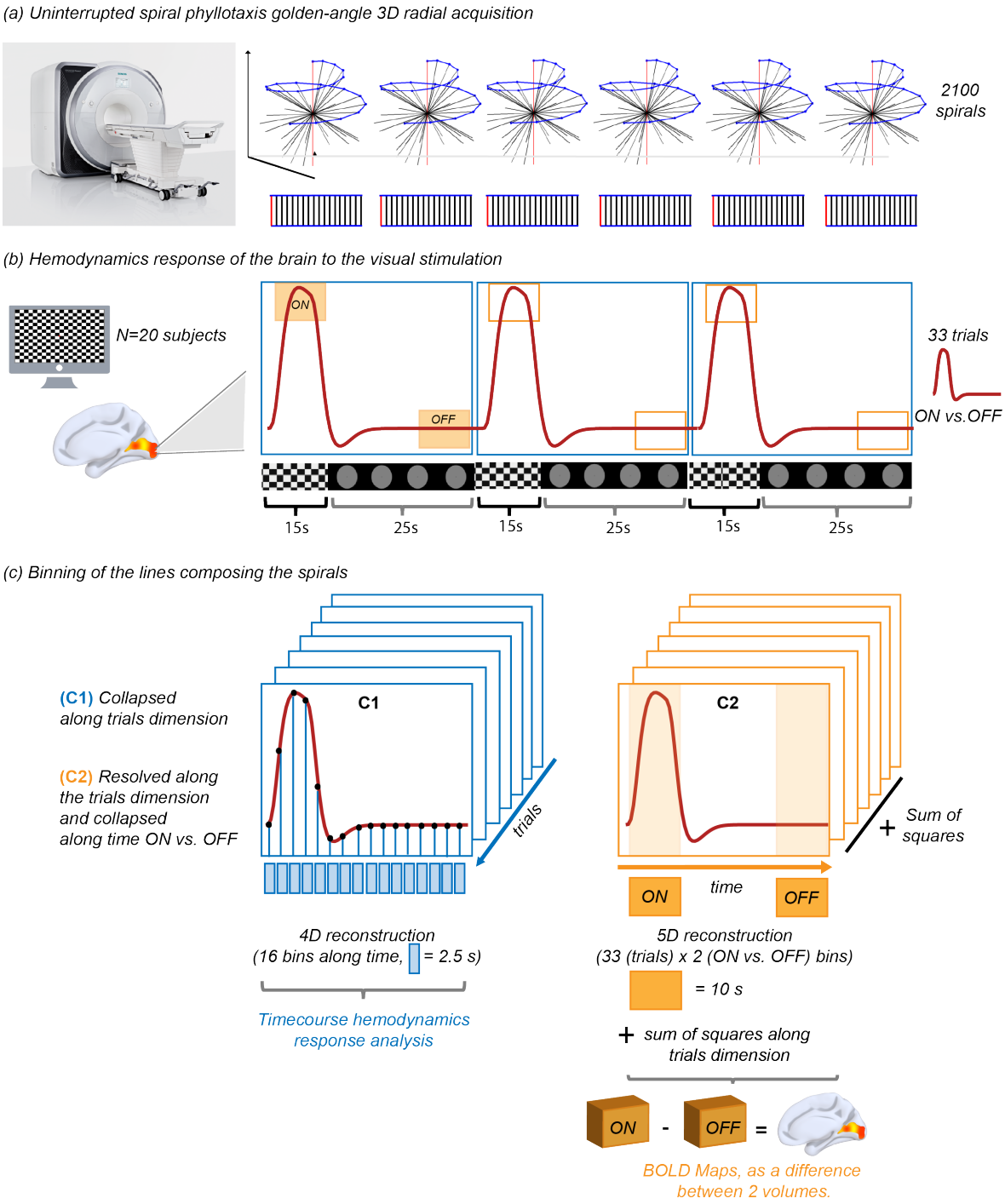

Figure 4. Overview of acquisition and reconstruction methods. A) The participant is placed in the scanner where we start acquiring data using a prototype uninterrupted gradient recalled echo (GRE) sequence with a 3D radial spiral phyllotaxis sampling trajectory, for a total of 46'772 readouts acquired. Every readout corresponds to a red (first line of the spiral acquired) or black segment as plotted below each spiral (interleave). **B)** During the acquisition, the participant views a flickering checkerboard that followed a blocked-deisgn (i.e., 15s ON vs. 25s OFF). Roughly 5s after the visual stimulation onset, the hemodynamic response within the primary visual cortex reaches its peak. **C)** We performed different types of reconstructions. C1 - blue) refers to the temporal reconstructions: we averaged across all trials, every trial being divided into temporal bins of different temporal sizes: 2.5s, 1s, 500ms, 250ms. This produced a four-dimensional reconstruction (x, y, z, t) along the averaged signal evolution curve. This allows us to analyze the evolution of the %-signal change at different sub-second temporal resolutions. C2 - orange) refers to the 5D reconstruction: the ON-phase was reconstructed by retaining readouts acquired over the 5-15s post-stimulus time interval (ON-phase), and readouts acquired over the 30-40s post-stimulus interval (for the OFF-phase). All other readouts were discarded. ON and OFF 3D volumes across different trials were then unified via sum of squares. $T_2{}^*$-weighted volume at the single participant level are computed as a pure mathematical difference between the sum of squared ON and OFF, i.e. $||ON - OFF||$.

Table 1. Reconstruction time of the different volumes In this table we list the reconstruction times measured with a workstation equipped with two Intel Xeon CPUs, 512GB of RAM, and an NVIDIA Tesla GPU, as well as the parameters used for image reconstruction. **CS** stands for Compressed-sensing, **TI** stands for Temporal Interval.

Type of reconstruction	Time	Parameters λ	Parameters ρ
5D-all [3D volumes x **33 Trials** x 2 Activation (ON-OFF)]	2h	$\lambda = 0.01$	$\rho = 0.06$
no-CS [**no CS**: 3D volumes x **33 Trials** x 2 Activation (ON-OFF)]	15min	$\lambda = 0.01$	$\rho = 0.06$
5D-half [3D volumes x **17 Trials** x 2 Activation (ON-OFF)]	1h30m	$\lambda = 0.01$	$\rho = 0.06$
4D-all [3D volumes x Averaged TI: **2.5s** resolution]	1h30m	$\lambda = 0.01$	$\rho = 0.06$
4D-all [3D volumes x Averaged TI: **1s** resolution]	2h16m	$\lambda = 0.01$	$\rho = 0.06$
4D-all [3D volumes x Averaged TI: **0.5s** resolution]	5h10m	$\lambda = 0.01$	$\rho = 0.06$
4D-all [3D volumes x Averaged TI: **0.250s** resolution]	13h20m	$\lambda = 0.01$	$\rho = 0.06$

Acknowledgements

Financial support for this work has been provided by the Fondation Asile des aveugles (grant #232933 to M.M.M.), a grantor advised by Carigest SA (#232920 to M.M.M.), as well as the Swiss National Science Foundation (grants #169206 to M.M.M., #173129, #150828, and #143923 to M.S.). M.N. was supported by the Alexander von Humboldt Foundation and by the Intramural Research Program of the NIMH (ZIAMH002909). We thank Antoine Lutti and Quentin Reynaud for the fruitful discussions around the results of this article and its future applicability.

Authors contributions

B.F. conceptualized the problem with advice from M.M.M and E.F. B.F. and E.F. developed, implemented, and tested the protocol. B.F. performed the data analysis and image reconstruction with advice from M.N. and M.M.M. S.R. and M.D. set up the framework for image reconstruction. T.H. and T.K. provided technical support to derive the acquisition parameters at the scanner console, as well as to determine the sequence and its specifications. C.W.R. performed the motion correction. G.D. performed the LGN extraction and contributed to the group-level analysis. R.v.H, M.S. and J.Y. contributed to formalizing the use of the compressed-sensing framework. G.P. contributed to the design of the network analysis techniques and interpretation. B.F., M.N., M.M.M. and E.F. drafted the manuscript, and all authors contributed to internal review.

Competing interests

B.F., J.Y., M.S., and M.M.M. declare the following competing financial interest: a patent application partially inspiring the protocol described in this manuscript has been published (WO/2020/178397). T.H. and T.K. are employed by Siemens Healthineers International AG. MS receives non-financial research support from Siemens Healthineers.

References

1. Ogawa, S., Lee, T.-M., Nayak, A. S. & Glynn, P. Oxygenation-sensitive contrast in magnetic resonance image of rodent brain at high magnetic fields. *Magn. Reson. Medicine* **14**, 68–78, DOI: 10.1002/mrm.1910140108 (1990).

2. Ogawa, S. *et al.* Intrinsic signal changes accompanying sensory stimulation: functional brain mapping with magnetic resonance imaging. *Proc. Natl. Acad. Sci.* **89**, 5951–5955, DOI: 10.1073/pnas.89.13.5951 (1992).

3. Belliveau, J. *et al.* Functional mapping of the human visual cortex by magnetic resonance imaging. *Science* **254**, 716–719, DOI: 10.1126/science.1948051 (1991).

4. Kwong, K. K. *et al.* Dynamic magnetic resonance imaging of human brain activity during primary sensory stimulation. *Proc. Natl. Acad. Sci.* **89**, 5675–5679 (1992).

5. Stehling, M. K., Turner, R. & Mansfield, P. Echo-planar imaging: magnetic resonance imaging in a fraction of a second. *Science* **254**, 43–50 (1991).

6. Mansfield, P. Multi-planar image formation using nmr spin echoes. *J. Phys. C: Solid State Phys.* **10**, L55 (1977).

7. Bandettini, P. A., Wong, E. C., Hinks, R. S., Tikofsky, R. S. & Hyde, J. S. Time course epi of human brain function during task activation. *Magn. resonance medicine* **25**, 390–397 (1992).

8. Van Essen, D. C. *et al.* The human connectome project: a data acquisition perspective. *Neuroimage* **62**, 2222–2231 (2012).

9. Bollmann, S. & Barth, M. New acquisition techniques and their prospects for the achievable resolution of fmri. *Prog. neurobiology* **207**, 101936 (2021).

10. Setsompop, K., Feinberg, D. A. & Polimeni, J. R. Rapid brain mri acquisition techniques at ultra-high fields. *NMR Biomed.* **29**, 1198–1221 (2016).

11. Larkman, D. J. *et al.* Use of multicoil arrays for separation of signal from multiple slices simultaneously excited. *J. Magn. Reson. Imaging: An Off. J. Int. Soc. for Magn. Reson. Medicine* **13**, 313–317 (2001).

12. Moeller, S. *et al.* Multiband multislice ge-epi at 7 tesla, with 16-fold acceleration using partial parallel imaging with application to high spatial and temporal whole-brain fmri. *Magn. resonance medicine* **63**, 1144–1153 (2010).

13. Poser, B. A., Koopmans, P. J., Witzel, T., Wald, L. L. & Barth, M. Three dimensional echo-planar imaging at 7 tesla. *Neuroimage* **51**, 261–266 (2010).

14. Posse, S. *et al.* Enhancement of temporal resolution and bold sensitivity in real-time fmri using multi-slab echo-volumar imaging. *Neuroimage* **61**, 115–130 (2012).

15. Wiesinger, F., Menini, A. & Solana, A. B. Looping star. *Magn. resonance medicine* **81**, 57–68 (2019).

16. Petrov, A. Y., Herbst, M. & Stenger, V. A. Improving temporal resolution in fmri using a 3d spiral acquisition and low rank plus sparse (l+ s) reconstruction. *Neuroimage* **157**, 660–674 (2017).

17. Martuzzi, R. *et al.* Multisensory interactions within human primary cortices revealed by bold dynamics. *Cereb. Cortex* **17**, 1672–1679 (2007).

18. Menon, R. S., Luknowsky, D. C. & Gati, J. S. Mental chronometry using latency-resolved functional mri. *Proc. Natl. Acad. Sci.* **95**, 10902–10907 (1998).

19. Graedel, N. N., Miller, K. L. & Chiew, M. Ultrahigh resolution fmri at 7t using radial-cartesian turbine sampling. *Magn. Reson. Medicine* **88**, 2058–2073 (2022).

20. Toi, P. T. *et al.* In vivo direct imaging of neuronal activity at high temporospatial resolution. *Science* **378**, 160–168 (2022).

21. Yang, Z. & Lewis, L. D. Imaging the temporal dynamics of brain states with highly sampled fmri. *Curr. opinion behavioral sciences* **40**, 87–95 (2021).

22. Lee, C. S. *et al.* Associations between recent and established ophthalmic conditions and risk of Alzheimer's disease. *Alzheimer's & dementia : journal Alzheimer's Assoc.* **15**, 34–41, DOI: 10.1016/j.jalz.2018.06.2856 (2019).

23. Cabral, J., Fernandes, F. F. & Shemesh, N. Intrinsic macroscale oscillatory modes driving long range functional connectivity in female rat brains detected by ultrafast fmri. *Nat. Commun.* **14**, 375 (2023).

24. Chuang, K.-H., Li, Z., Huang, H. H., Khorasani Gerdekoohi, S. & Athwal, D. Hemodynamic transient and functional connectivity follow structural connectivity and cell type over the brain hierarchy. *Proc. Natl. Acad. Sci.* **120**, e2202435120 (2023).

25. Engel, S. A., Glover, G. H. & Wandell, B. A. Retinotopic organization in human visual cortex and the spatial precision of functional mri. *Cereb. cortex (New York, NY: 1991)* **7**, 181–192 (1997).

26. Piccini, D., Littmann, A., Nielles-Vallespin, S. & Zenge, M. O. Spiral phyllotaxis: the natural way to construct a 3d radial trajectory in mri. *Magn. resonance medicine* **66**, 1049–1056 (2011).

27. Buckner, R. L. Event-related fmri and the hemodynamic response. *Hum. brain mapping* **6**, 373–377 (1998).

28. DeYoe, E. A., Bandettini, P., Neitz, J., Miller, D. & Winans, P. Functional magnetic resonance imaging (fmri) of the human brain. *J. neuroscience methods* **54**, 171–187 (1994).

29. DeYoe, E. A. & Raut, R. V. Visual mapping using blood oxygen level dependent functional magnetic resonance imaging. *Neuroimaging Clin.* **24**, 573–584 (2014).

30. Murphy, K., Bodurka, J. & Bandettini, P. A. How long to scan? the relationship between fmri temporal signal to noise ratio and necessary scan duration. *Neuroimage* **34**, 565–574 (2007).

31. Dale, A. M. & Buckner, R. L. Selective averaging of rapidly presented individual trials using fmri. *Hum. brain mapping* **5**, 329–340 (1997).

32. Burock, M. A., Buckner, R. L., Woldorff, M. G., Rosen, B. R. & Dale, A. M. Randomized event-related experimental designs allow for extremely rapid presentation rates using functional mri. *Neuroreport* **9**, 3735–3739 (1998).

33. Kastner, S. *et al.* Functional imaging of the human lateral geniculate nucleus and pulvinar. *J. neurophysiology* **91**, 438–448 (2004).

34. Kastner, S., Schneider, K. A. & Wunderlich, K. Beyond a relay nucleus: neuroimaging views on the human lgn. *Prog. brain research* **155**, 125–143 (2006).

35. Smith, S. M. & Nichols, T. E. Threshold-free cluster enhancement: addressing problems of smoothing, threshold dependence and localisation in cluster inference. *Neuroimage* **44**, 83–98 (2009).

36. Lustig, M., Donoho, D., Santos, J. & Pauly, J. Compressed Sensing MRI. *IEEE Signal Process. Mag.* **25**, 72–82, DOI: 10.1109/MSP.2007.914728 (2008).

37. Wennerberg, A. B., Jonsson, T., Forssberg, H. & Li, T.-Q. A comparative fmri study: T 2*-weighted imaging versus r 2* mapping. *NMR Biomed. An Int. J. Devoted to Dev. Appl. Magn. Reson. In Vivo* **14**, 41–47 (2001).

38. Ekman, M., Kok, P. & de Lange, F. P. Time-compressed preplay of anticipated events in human primary visual cortex. *Nat. Commun.* **8**, 15276 (2017).

39. Kasper, L. *et al.* Advances in spiral fmri: a high-resolution study with single-shot acquisition. *NeuroImage* **246**, 118738 (2022).

40. Glover, G. H. Spiral imaging in fmri. *Neuroimage* **62**, 706–712 (2012).

41. Chen, W. *et al.* Mapping of lateral geniculate nucleus activation during visual stimulation in human brain using fmri. *Magn. resonance medicine* **39**, 89–96 (1998).

42. O'Connor, D. H., Fukui, M. M., Pinsk, M. A. & Kastner, S. Attention modulates responses in the human lateral geniculate nucleus. *Nat. neuroscience* **5**, 1203–1209 (2002).

43. Jeromin, O., Pattichis, M. S. & Calhoun, V. D. Optimal compressed sensing reconstructions of fmri using 2d deterministic and stochastic sampling geometries. *Biomed. engineering online* **11**, 1–36 (2012).

44. Holland, D. *et al.* Compressed sensing reconstruction improves sensitivity of variable density spiral fmri. *Magn. Reson. Medicine* **70**, 1634–1643 (2013).

45. Gross, J. Magnetoencephalography in cognitive neuroscience: a primer. *Neuron* **104**, 189–204 (2019).

46. Biasiucci, A., Franceschiello, B. & Murray, M. M. Electroencephalography. *Curr. Biol.* **29**, R80–R85 (2019).

47. Haak, K. V., Marquand, A. F. & Beckmann, C. F. Connectopic mapping with resting-state fmri. *Neuroimage* **170**, 83–94 (2018).

48. Goense, J., Merkle, H. & Logothetis, N. K. High-resolution fmri reveals laminar differences in neurovascular coupling between positive and negative bold responses. *Neuron* **76**, 629–639 (2012).

49. Magri, C., Logothetis, N. K. & Panzeri, S. Investigating static nonlinearities in neurovascular coupling. *Magn. Reson. Imaging* **29**, 1358–1364 (2011).

50. Jafarian, A., Litvak, V., Cagnan, H., Friston, K. J. & Zeidman, P. Comparing dynamic causal models of neurovascular coupling with fmri and eeg/meg. *NeuroImage* **216**, 116734 (2020).

51. Logothetis, N. K., Pauls, J., Augath, M., Trinath, T. & Oeltermann, A. Neurophysiological investigation of the basis of the fmri signal. *nature* **412**, 150–157 (2001).

52. Marek, S. *et al.* Reproducible brain-wide association studies require thousands of individuals. *Nature* **603**, 654–660 (2022).

53. Eippert, F., Kong, Y., Jenkinson, M., Tracey, I. & Brooks, J. C. Denoising spinal cord fmri data: Approaches to acquisition and analysis. *Neuroimage* **154**, 255–266 (2017).

54. Stroman, P. W. Magnetic resonance imaging of neuronal function in the spinal cord: spinal fmri. *Clin. medicine & research* **3**, 146–156 (2005).

55. Powers, J. M., Ioachim, G. & Stroman, P. W. Ten key insights into the use of spinal cord fmri. *Brain sciences* **8**, 173 (2018).

56. Frey, M., Nau, M. & Doeller, C. F. Magnetic resonance-based eye tracking using deep neural networks. *Nat. neuroscience* **24**, 1772–1779 (2021).

57. Franceschiello, B. *et al.* 3-Dimensional magnetic resonance imaging of the freely moving human eye. *Prog. Neurobiol.* 101885, DOI: 10.1016/j.pneurobio.2020.101885 (2020).

58. Kirchner, J., Watson, T. & Lappe, M. Real-time mri reveals unique insight into the full kinematics of eye movements. *Eneuro* **9** (2022).

59. Sengupta, S., Smith, D. S., Smith, A. K., Welch, E. B. & Smith, S. A. Dynamic imaging of the eye, optic nerve, and extraocular muscles with golden angle radial MRI. *Investig. Ophthalmol. Vis. Sci.* **58**, 4010–4018, DOI: 10.1167/iovs.17-21861 (2017).

60. Coppo, S. *et al.* Free-running 4D whole-heart self-navigated golden angle MRI: Initial results. *Magn. Reson. Medicine* **74**, 1306–1316, DOI: 10.1002/mrm.25523 (2015).

61. Lorenzo Di Sopra, Davide Piccini, Simone Coppo, Matthias Stuber, J. Y. An automated approach to fully self-gated free-running cardiac and respiratory motion-resolved 5D whole-heart MRI. *Magn. Reson. Medicine* (2019).

62. Penny, W. D., Friston, K. J., Ashburner, J. T., Kiebel, S. J. & Nichols, T. E. *Statistical parametric mapping: the analysis of functional brain images* (Elsevier, 2011).

63. Fischl, B. Freesurfer. *Neuroimage* **62**, 774–781 (2012).

Supplementary material

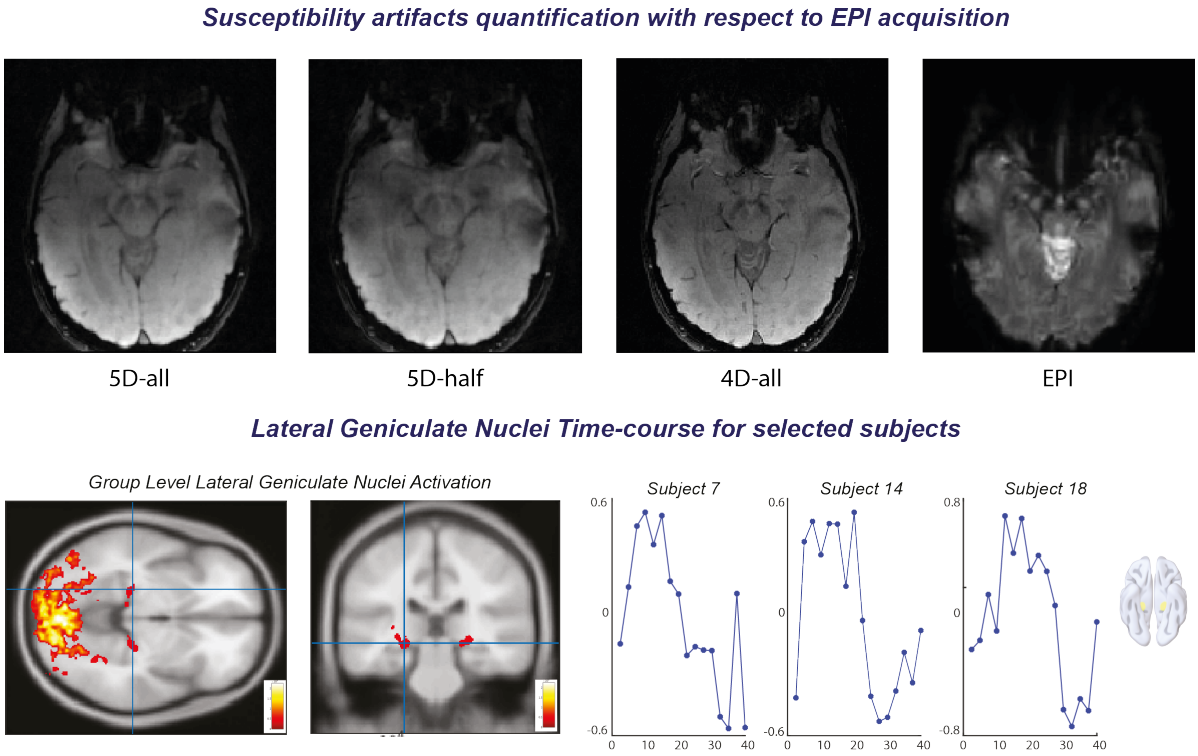

Figure 5. Top row: susceptibility artifacts quantification with respect to EPI acquisition. One subject underwent our protocol, together with an EPI (TR=2s, TE=73ms, FA=80°, resolution 2x2x3mm, TA=5.06min, Slices=14). A mask was created to isolate gray-matter in the selected axial slice after co-registration (the axial slice is therefore common to all four volumes, i.e. our three reconstruction and the slab acquired via EPI). We computed and report the coefficient of variation (CV) as a direct measure of the susceptibility artifacts magnitude across our reconstruction and the EPI. The measured CV is the following: 5D-all=0.407, 5D-half=0.435, 4D-all=0.351 and EPI=0.51. EPI reports the highest CV value.
Bottom row: activation in LGN. In the 5D-all reconstruction we could observe hemodynamic responses in the lateral geniculate nuclei, i.e. thalamic subnuclei. We conducted an analysis at the single participant level, reporting here the three participants with the strongest percent signal change (around 0.8%).